



Full Length Article

Chemically stable $TMO_x@Ti\text{-MgO}$ ($TM = \text{Mn}$ and Cu) catalyst enhanced De/hydrogenation kinetics of Mg/MgH_2

Haotian Guan^a, Jiang Liu^a, Qian Li^{a,b}, Yangfan Lu^{a,b,*}, Fusheng Pan^{a,b}

^aCollege of Materials Science and Engineering, National Engineering Research Center for Mg Alloys, National Key Laboratory of Advanced Casting Technologies, National Innovation Center for Industry-Education Integration of Energy Storage Technology, Chongqing University, Chongqing 400045, China

^bChongqing Institute of New Energy Storage Materials and Equipment, Chongqing 401135, China

Received 14 November 2024; received in revised form 5 February 2025; accepted 26 February 2025

Available online xxx

Abstract

Ti-based catalysts have been identified to be efficient in enhancing hydrogenation and dehydrogenation (de/hydrogenation) kinetics of Mg/MgH_2 . However, their catalytic activity is constrained by the strong Ti–H bond and chemical instability. Herein, we demonstrate that $TMO_x@Ti\text{-MgO}$ ($TM = \text{Mn}$ and Cu) composite catalysts can simultaneously enhance hydrogen dissociation, diffusion and nucleation processes. MgH_2 catalyzed by $TMO_x@Ti\text{-MgO}$ released 6.03–6.14 wt. % H_2 within 5 min at 280 °C and 0.89–1.12 wt. % H_2 within 60 min at 180 °C. The partially oxidized Ti^{2+} and Ti^{3+} states are stabilized in MgO lattice, accelerating hydrogen adsorption, dissociation and diffusion processes. The TMO_x , additionally, serve as the active center for nucleation, further improving de/hydrogenation reactions. The $TMO_x@Ti\text{-MgO}$ catalysts are characterized by high chemical stability, realizing improved cycle properties. These findings suggest a new approach to achieving controllable Catalyst-Hydrogen bond strengths and optimizing performance in de/hydrogenation reactions.

© 2025 Chongqing University. Publishing services provided by Elsevier B.V. on behalf of KeAi Communications Co. Ltd.

This is an open access article under the CC BY-NC-ND license (<http://creativecommons.org/licenses/by-nc-nd/4.0/>)

Peer review under responsibility of Chongqing University

Keywords: Ti-based catalyst; Mg/MgH_2 ; hydrogen storage; hydrogen diffusion; nucleation.

1. Introduction

Safe and efficient hydrogen storage and transport techniques are essential for further developing hydrogen energy industries. Compared to gaseous and liquid hydrogen storage, solid-state hydrogen storage techniques offer more safety and higher hydrogen storage capacity. Among the various hydrogen storage materials, magnesium hydride (MgH_2) has drawn considerable attention owing to its high hydrogen storage capacity (7.6 wt. %), abundant resources, and environmentally friendly properties [1–3]. However, the practical application of MgH_2 is hindered by its inherent sluggish kinetics and poor cycling stability [4–6].

The hydrogen storage mechanism in Mg-based materials mainly involves hydrogen adsorption, dissociation, diffusion

and nucleation processes [2,7]. On the surface of pure Mg, hydrogen dissociation step is considered the rate-determining step (RDS), whose activation barrier is as high as ~1.4 eV [8]. To accelerate this step, various transition metal-based catalysts have been developed [9–12]. These catalysts interact with hydrogen by forming catalyst–hydrogen (Cat–H) bonds, thereby weakening the H–H bond strength [13,14]. Ti-based compounds, which can create Ti–H bond, thus emerged as promising candidates in this context [12,15–17]. Nonetheless, the excessively Ti–H bonds result in high hydrogen diffusion barrier, which is known as the scaling limitation. In addition, Ti-based compounds are characterized by multiple valence state natures and poorer chemical stability. This poses a major challenge for designing controllable and robust Ti-based catalysts for Mg-based hydrogen storage materials [18,19].

Recent studies suggest that doping early transition metals, such as Ti, V and Nb, into MgO can enhance the catalysts' chemical and structural durability [20]. In these systems, Ti

* Corresponding author.

E-mail address: yangfanlu@cqu.edu.cn (Y. Lu).

acts as the catalytically active sites while V and Nb serve as the stabilizer in TiV-MgO and TiNb-MgO [20]. Therefore, although TiV-MgO and TiNb-MgO can efficiently accelerate hydrogen dissociation and diffusion processes, their contribution to the subsequent processes, such as Mg/MgH₂ nucleation, is insufficient [20]. The incorporation of late transition metal oxides such as MnO or CuO into the Mg/MgH₂ system significantly enhances hydrogen diffusion and nucleation processes by creating additional pathways and sites for the kinetic processes [21,22]. This multiphase catalytic environment not only lowers the energy barriers associated with hydrogen absorption and desorption but also accelerates the phase transformation kinetics, thereby improving the overall performance of hydrogen storage systems. Thus, we are motivated to investigate the impact of Ti-MgO and combine middle/late transition metal catalysts on the hydrogenation and dehydrogenation (de/hydrogenation) kinetics of Mg/MgH₂ [21–23].

Herein, we demonstrate that the $TMO_x@Ti\text{-MgO}$ in Mg/MgH₂ facilitates concurrent enhancement of hydrogen dissociation, diffusion and nucleation processes. With $TiTMO_4$ ($TM = \text{Mn and Cu}$) as the precursor, Ti-MgO and TMO_x nanoparticles are uniformly distributed within MgH₂, thereby achieving robust Ti and TM chemical properties. MgH₂ catalyzed by $TMO_x@Ti\text{-MgO}$ ($TMO_x@Ti\text{-MgO/MgH}_2$) released 6.03–6.14 wt. % H₂ at 280 °C within 5 min and 0.89–1.12 wt. % at 180 °C within 60 min. XRD, TEM, and XPS analyses revealed that the chemical and structural morphology of $TMO_x@Ti\text{-MgO}$ catalysts remained largely stable after 30 cycles. Kinetic analysis shows that the nucleation step is no longer the rate-determining step (RDS) of de/hydrogenation reactions, indicating that TMO_x nanoparticles contribute to accelerating the process. These findings suggest the synergistic effect between early and middle/late transition metals offers a promising catalyst design concept for reversible de/hydrogenation reactions.

2. Experimental methods

Synthesis of $TiTMO_4$ ($TM = \text{Mn and Cu}$) precursor

Titanium sulfate (Ti(SO₄)₂, 96 %), manganese chloride hydrate (MnCl₂·4H₂O, 99 %), copper chloride (CuCl₂, 98 %), and urea (CO(NH₂)₂) were obtained from Macklin. Initially, 0.003 mol of Ti(SO₄)₂ and 0.003 mol of either MnCl₂ or CuCl₂ were sequentially added to 25 ml of deionized water, followed by thorough stirring for 5 min at room temperature. Subsequently, an excessive amount of urea solution was introduced into the mixture. The homogeneously mixed solution underwent reaction in a 100 ml autoclave at 90 °C for 24 h. Ultimately, the resultant precipitate was subjected to several rounds of centrifugation, alternating between deionized water and ethanol. Following centrifugation, the product was dried at 80 °C for 6 h and then heat-treated at 450 °C for 2 h to yield the $TiTMO_4$ precursor. XRD, SEM and XPS results of the $TiTMO_4$ precursor are shown in Fig. S1–S5.

Preparation of $TMO_x@Ti\text{-MgO/Mg}$ composites

The $TiTMO_4$ ($TM = \text{Mn and Cu}$) precursor was incorporated into MgH₂ via high-energy ball milling. Then, the mixture was subjected to ball milling at a speed of 400 rpm for 20 h, maintaining a ball-to-sample ratio of 20:1. To mitigate the risk of overheating, a pause of 10 min was mandated after each 10-minute milling interval. The ball-milled samples are denoted as $TiTMO_4/\text{MgH}_2$. After the dehydrogenation process, the $TMO_x@Ti\text{-MgO}$ catalysts are obtained on the surface of Mg (Fig. S1).

Characterization methods

The phase structure and morphology of the samples were characterized through X-ray diffraction (XRD, PANalytical Empyrean, Cu K α) and scanning electron microscopy (SEM, Zeiss Sigma 300) equipped with an energy dispersive spectrometer (EDS, Oxford Xplore 30), respectively. Transmission electron microscopy (TEM, Talos F200S) were used to observe the morphology, elemental distribution and high-resolution lattice of the samples. The crystalline phases were identified by using the ICDD database and quantified by Rietveld refinement with GSAS software. X-ray photoelectron spectroscopy (XPS) measurements were conducted on an X-ray photoelectron spectrometer (Thermo Scientific K-Alpha Nexsa) at a base pressure of 5.0×10^{-10} mbar. All XPS data fitting was done in XPSPEAK41 software, combined with an energy correction based on the C 1 s signal at 284.8 eV.

Hydrogen storage performance measurements

Isothermal hydrogenation and dehydrogenation curves as well as hydrogen desorption and adsorption cycle curves, were obtained with the commercial Sieverts-type apparatus (PCT pro, Setaram). The background hydrogen pressure was set to 30 bar for the hydrogen absorption process and 0.01 bar for the dehydrogenation process. The cycling test was 20 min for adsorption and 10 min for desorption. To better understand the dehydrogenation kinetic behavior of $TMO_x@Ti\text{-MgO/MgH}_2$ composites, the equations associated with Sharps and Jones method was used to fit the isothermal dehydrogenation curves at different temperatures: [24,25]

$$\frac{d\alpha}{dt} = kf(\alpha) \quad (1)$$

$$f(\alpha) = A(t/t_{0.5}) \quad (2)$$

where α is the reaction extent, k is the reaction rate constant, $f(\alpha)$ is a function that depends on a specific kinetic mechanism, A represents a constant related to the kinetic mechanism, and $t_{0.5}$ represents the time when α equals to 0.5. The kinetic model is obtained by plotting the experimental value ($t/t_{0.5}$)_{exp} against the theoretical value ($t/t_{0.5}$)_{theo}.

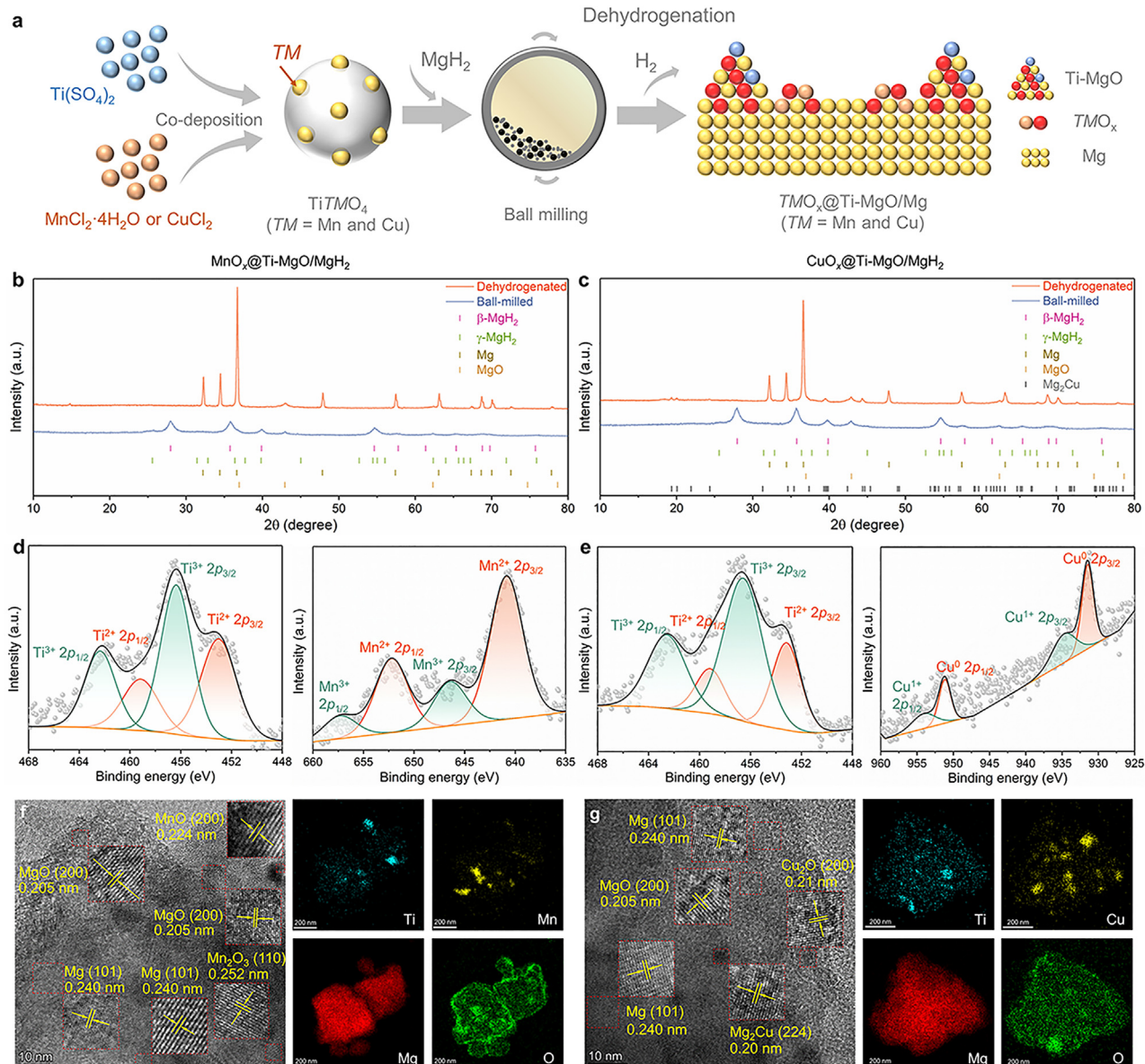


Fig. 1. (a) Synthesis process illustration and (b and c) XRD patterns of the ball-milled and dehydrogenated TMO_x@Ti-MgO catalyzed MgH₂. (d and e) High-resolution Ti 2p, Mn 2p and Cu 2p spectra of TMO_x@Ti-MgO/MgH₂ at different states. (f and g) HAADF images of dehydrogenated TMO_x@Ti-MgO/MgH₂ and corresponding EDS elemental mapping results.

3. Results and discussion

3.1. Structure and electronic properties of the catalysts

The preparation process of the TMO_x@Ti-MgO/MgH₂ composite is depicted in Fig. 1a. XRD patterns of the pristine TiTMO₄ (TM = Mn and Cu) shown in Fig. S2 reveal their anatase structure (JCPDS No 21-1272), with minor phases of MnO₂ and CuO. SEM-EDS mapping (Fig. S3 and S4) confirms a uniform distribution of Ti within the anatase, MnO₂, and CuO phases, as well as TM elements in TiTMO₄. The XPS spectra presented in Fig. S5 indicate that the valence states of Ti and Mn in TiMnO₄ are Ti⁴⁺ and Mn³⁺, respectively. Additionally, for TiCuO₄, the va-

lence states of Ti and Cu are identified as Ti⁴⁺, Cu²⁺ and Cu¹⁺. XRD results of TiTMO₄/MgH₂ before and after dehydrogenation are displayed in Fig. 1b and c. The ball-milled TiTMO₄/MgH₂ composites predominantly consist of β-MgH₂ and γ-MgH₂ phases, with no obvious peaks of TiTMO₄. Although MgH₂ peaks are retained, a minor amount of MgO is also detected, indicating a redox reaction between TiTMO₄ and MgH₂ during ball milling. This process results in the finely dispersed and catalytically active metal TM-doped inert MgO. Fig. S6 and S7 show SEM-EDS results of the ball-milled TiTMO₄/MgH₂, illustrating a uniform distribution of O, Mg, Ti, and TM elements after ball milling. In the dehydrogenated TiTMO₄/MgH₂, MgH₂ peaks disappeared, and the Mg was found to be the major phase. The MgO phase re-

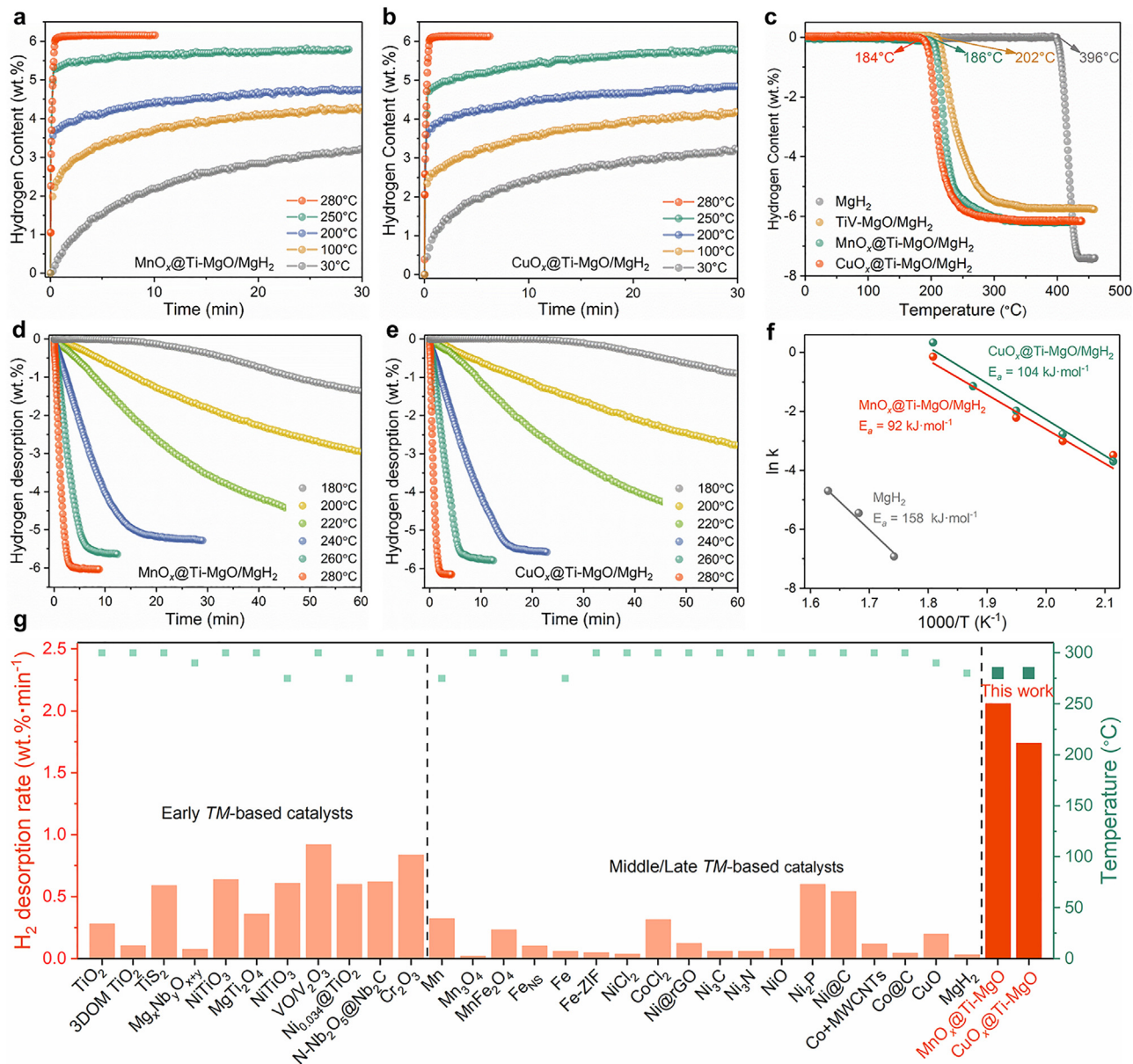


Fig. 2. (a and b) Isothermal H₂ absorption curves of TMO_x@Ti-MgO/Mg at various temperatures. (c) TPD results of the TMO_x@Ti-MgO/MgH₂ samples. (d-f) Isothermal dehydrogenation profiles and activation energies (calculated by the R2 model) of TMO_x@Ti-MgO/MgH₂ composites. (g) Comparison of the initial desorption rates of TMO_x@Ti-MgO/MgH₂ composites with those of other Ti species catalyzed MgH₂ systems and transition metal catalyzed MgH₂ systems.

mains stable throughout the ball-milled and dehydrogenation processes. Based on these observations, it can be deduced that TiTMO₄ is reduced by MgH₂ during the ball milling.

The valence state changes of Ti and transition metal (TM) elements in the dehydrogenated TiTMO₄/MgH₂ composites were analyzed using X-ray photoelectron spectroscopy (XPS). XPS data (Figs. 1d and e) reveal partial oxidation of Ti sites, showing valence states of Ti²⁺ and Ti³⁺, which is consistent with the incorporation of Ti into MgO to form Ti-MgO catalysts [20]. The valence states of Mn were estimated as Mn²⁺ and Mn³⁺, while Cu¹⁺ and Cu⁰ was observed for Cu. TEM-EDS results indicate a distinct distribution of TM elements compared to Ti (Fig. 1f and g), illustrating TMO_x

phases formed in addition to Ti-MgO. HAADF-STEM and corresponding EDS images display a uniform distribution of MgO on MgH₂, with particle sizes ranging from 60 to 100 nm (Fig. 1f and g). These findings indicate that TMO_x@Ti-MgO catalysts can be synthesized effectively through the in-situ reduction of the TiTMO₄ precursor on the Mg/MgH₂ surface after dehydrogenation reaction.

3.2. De/hydrogenation properties and kinetic analysis

To further investigate the effects of TMO_x@Ti-MgO catalysts on Mg/MgH₂, isothermal hydrogen absorption and desorption measurements were conducted. Fig. 2a and b present

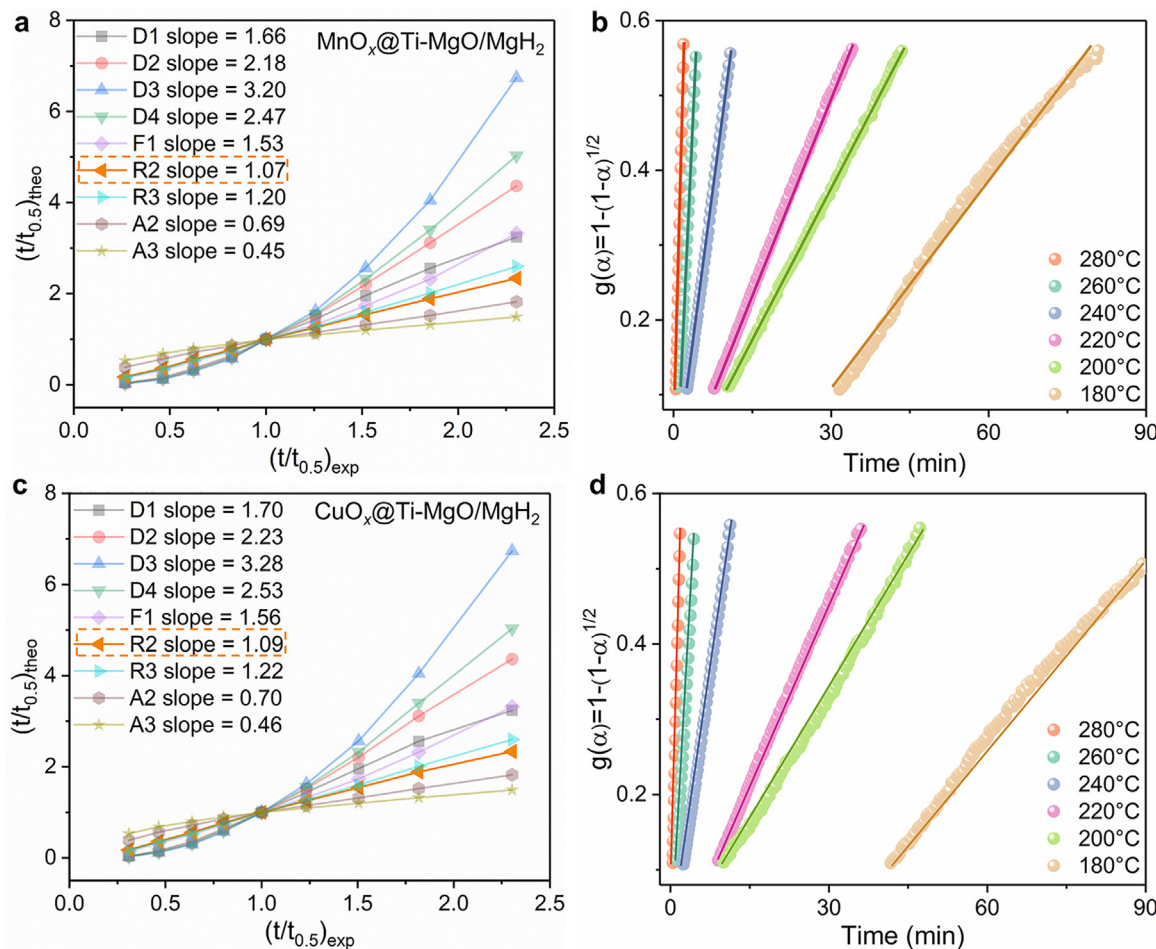


Fig. 3. (a and c) Various kinetic models of $TMO_x@Ti\text{-MgO}/MgH_2$ at 280 °C. (b and d) R2 model of $TMO_x@Ti\text{-MgO}/MgH_2$ at different temperatures.

the isothermal hydrogen absorption curves of the $TMO_x@Ti\text{-MgO}/Mg$ samples at 280 °C, 250 °C, 200 °C, 100 °C and 30 °C under 30 bar hydrogen pressure. The samples absorbed 3.25 wt. % H₂ within 30 min at 30 °C, and 6.18 wt. % H₂ at 280 °C within only 60s. After the absorption process, the temperature-programmed desorption (TPD) of the $TMO_x@Ti\text{-MgO}/MgH_2$ samples was examined. Pure MgH₂ began releasing hydrogen at 396 °C, and reached 7.56 wt. % H₂ at 430 °C. Notably, a temperature reduction of 212 °C and 210 °C was observed for CuO_x@Ti-MgO/MgH₂ and MnO_x@Ti-MgO/MgH₂, respectively (Fig. 2c). The dehydrogenation properties improved significantly with the introduction of the $TMO_x@Ti\text{-MgO}$ catalysts, as evidenced by the increased dehydrogenation rate (Fig. 2d and e). The $TMO_x@Ti\text{-MgO}/MgH_2$ composites released 6.03 wt. % H₂ and 6.14 wt. % H₂ within 5 min at 280 °C, respectively, representing improvements of 50–60 times over pure Mg/MgH₂.

Fig. 2g and Table S1 compare the hydrogen storage properties of MgH₂ with those of early transition metals [12,18,26–36], and middle/late transition metals [37–56]. The dehydrogenation rates remarkably exceed those previously reported for early and late transition metal catalysts, such as TiS₂ (0.59 wt. %·min⁻¹) [28], Mn₃O₄ (0.33 wt. %·min⁻¹) [39] and CuO (0.20 wt. %·min⁻¹) [56]. The improved re-

action kinetics is further supported by the activation energy values, which were calculated to be 92 kJ·mol⁻¹ for MnO_x@Ti-MgO/MgH₂ and 104 kJ·mol⁻¹ for CuO_x@Ti-MgO/MgH₂, respectively (Fig. 2f). These activation energy values are considerably lower than that of pure MgH₂, indicating that the $TMO_x@Ti\text{-MgO}$ catalysts significantly facilitate the hydrogen desorption process. Even at 180 °C, the MnO_x@Ti-MgO/MgH₂ and CuO_x@Ti-MgO/MgH₂ desorb nearly 1.12 wt. % H₂ and 0.89 wt. % H₂ in 60 min (Fig. 2d and e), respectively. The $TMO_x@Ti\text{-MgO}$ catalysts demonstrated higher efficiency than previously investigated TiV-MgO/MgH₂ and MgH₂ systems [20]. Compared with the reported high-performance catalysts [11,12,26,35], the $TMO_x@Ti\text{-MgO}$ catalysts has a lower initial hydrogen desorption temperature and a faster hydrogen desorption rate (Fig. S8). This enhancement is attributed to the formation of efficient hydrogen diffusion pathways at the MnO_x and CuO_x sites, substantiated by SEM-EDS, HAADF-STEM, and XPS analyses.

Isothermal kinetic models are indispensable for understanding the mechanisms of hydrogen absorption and desorption. To elucidate the kinetic mechanisms in $TMO_x@Ti\text{-MgO}/MgH_2$, nine kinetic models proposed by Sharp and Jones are employed to identify the rate-determining step dur-

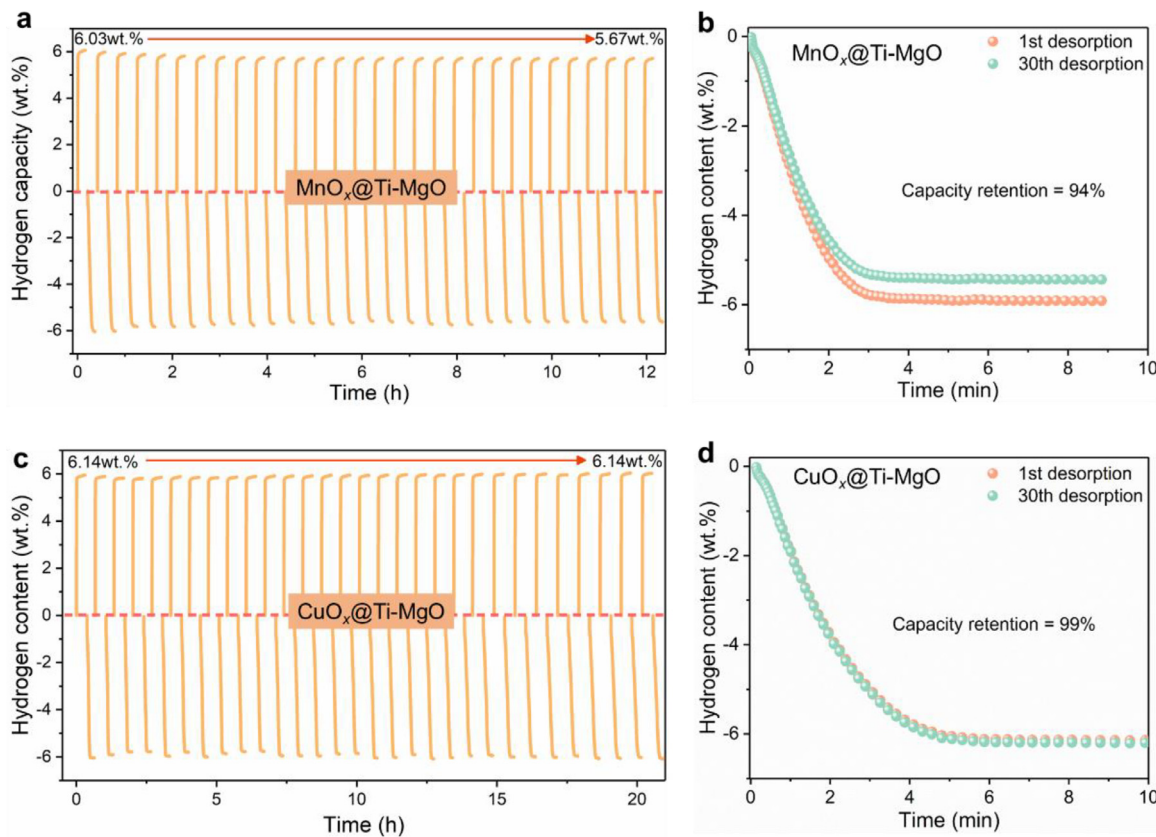


Fig. 4. (a and c) Reversible hydrogen absorption and desorption cycling profiles of $\text{TMO}_x@\text{Ti-MgO}/\text{MgH}_2$ at 280 °C. (b and d) Hydrogen desorption curves of $\text{TMO}_x@\text{Ti-MgO}/\text{MgH}_2$ at different cycles (1st and 30th).

ing hydrogen desorption (Fig. 3). In these models, the experimental value ($t/t_{0.5}\text{exp}$) is plotted and compared with the theoretical value ($t/t_{0.5}\text{theo}$). As illustrated in Fig. 3a and c, the R_2 model (two-dimensional phase boundary) proves is most suitable fitting for the dehydrogenated $\text{TMO}_x@\text{Ti-MgO}/\text{MgH}_2$, as its slope approaches 1. This precision is further corroborated by Fig. 3b and d. The R_2 model implies that the composite catalysts enhance hydrogen diffusion and nucleation sites, indicating that nucleation and growth within the Mg/MgH₂ system are enhanced by the catalyst incorporation.

3.3. Chemical and catalytic stability of the catalysts

Fig. 4 illustrates the isothermal hydrogen absorption and desorption behaviors of $\text{TMO}_x@\text{Ti-MgO}/\text{MgH}_2$ composites at 280 °C over 30 cycles. For the $\text{MnO}_x@\text{Ti-MgO}/\text{MgH}_2$ composite, a slight decrease in hydrogen storage capacity is observed during the first 5 cycles, likely due to particle aggregation (Fig. 4a and b). From the 5th to the 30th cycle, the capacity ranges from 6.03 wt. % H₂ to 5.67 wt. % H₂, maintaining a capacity retention rate of 94 %. Moreover, $\text{CuO}_x@\text{Ti-MgO}/\text{MgH}_2$ demonstrates negligible degradation, with a capacity from 6.14 wt. % to 6.12 wt. % after 30 cycles and achieved as high a capacity retention as 99 % (Fig. 4c and d). The dehydrogenation rates remained largely unchanged between the 1st and 30th cycle, showing high cycle stability

in terms of hydrogen storage capacity and reaction rates. These findings suggest the high chemical and catalytic stability of the catalysts.

To further reveal the origin of improved cycle stability the phase components, microstructure, and electronic properties of the cycled samples were investigated. The powder XRD patterns of the 1st and 30th dehydrogenated states of $\text{TMO}_x@\text{Ti-MgO}/\text{Mg}$ show that the peak position and peak widths of major phases (Mg) and the catalyst phases ($\text{TMO}_x@\text{Ti-MgO}$) remained largely unchanged (Fig. 5a and b). The particle size of $\text{TMO}_x@\text{Ti-MgO}$ range from 50 nm to 90 nm, slightly smaller than the starting materials, which may be due to mechanical degradation. The MgO (200) plane spacing is estimated to be 0.205 nm, consistent with the fresh sample, as shown in Fig. 5c and d. XPS measurements further analyze the valence states of Ti and TM in the Ti-MgO and TMO_x nanoparticles (Fig. 5e and f). The results show that Ti retains its valence states of Ti^{2+} and Ti^{3+} . No other oxidation states were identified. This indicates that the MgO lattice effectively stabilizes the chemical properties of Ti, preventing undesired reduction or oxidation during de/hydrogenation cycles. Collectively, the material structure and particle size of $\text{TMO}_x@\text{Ti-MgO}/\text{MgH}_2$ appear stable and consistent before and after hydrogen absorption and desorption cycles. Combined with XRD, XPS and TEM results, the introduction of Ti-MgO and TMO_x not only increases the number

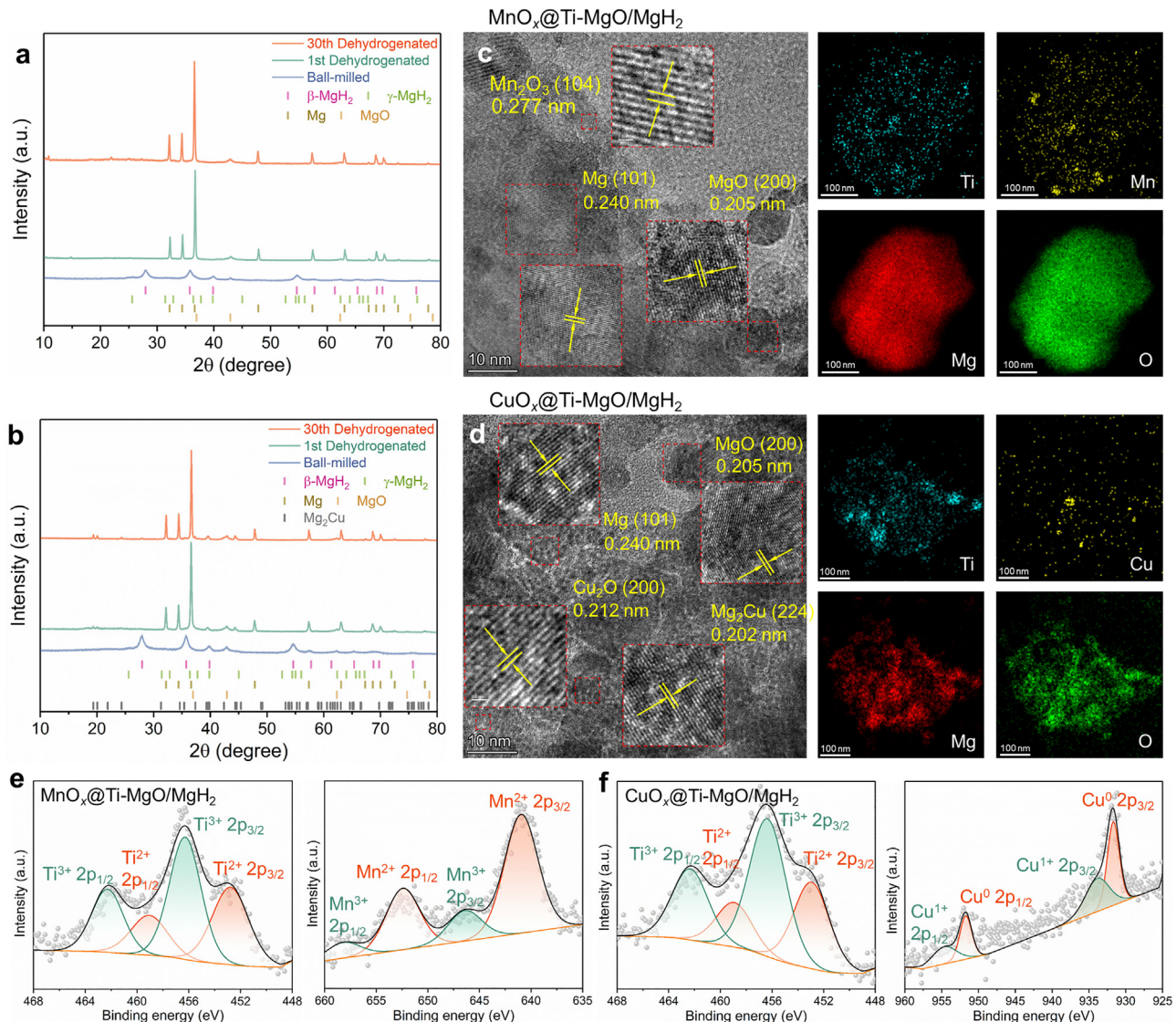


Fig. 5. (a and b) XRD patterns of ball-milled, the dehydrogenated state and cyclic dehydrogenated state of $\text{TMO}_x\text{@Ti-MgO/MgH}_2$. (c and d) High-resolution TEM images and the corresponding elemental mapping of 30th dehydrogenated $\text{TMO}_x\text{@Ti-MgO/MgH}_2$. (e and f) High-resolution XPS spectra of Ti 2p, Mn 2p and Cu 2p orbitals.

of active sites but may also stabilize the interfacial structure, mitigating the structural degradation of Mg/MgH₂ after 30 cycles.

Based on the above discussions, the catalytic mechanisms of $\text{TMO}_x\text{@Ti-MgO}$ can be summarized as follows. Initially, TiTMO_4 reacts with MgH₂ to form TiTM-MgO with ball milling. During dehydrogenation, TiTMO_4 were in-situ reduced by MgH₂, leading to the formation of $\text{TMO}_x\text{@Ti-MgO}$ composite catalysts. The DFT results show that MgO has weak interactions with hydrogen, making it unsuitable for hydrogen activation (Fig. S9). In contrast, on the pure Ti catalyst, hydrogen dissociates spontaneously due to the strong Ti-H bond, resulting in a high diffusion barrier of 1.26 eV. For the Ti-MgO catalyst, the Cat-H bond strengths are weaker than that of pure Ti, and the dissociated states are 1.04 eV more stable than the initial state (Fig. S9). This indicates

that Ti sites optimize the Cat-H bond strength, reducing the hydrogen dissociation barrier to 0.25 eV and the diffusion barrier to 0.57 eV, thus promoting efficient hydrogen adsorption, dissociation and diffusion simultaneously. TMO_x provides additional diffusion pathways and nucleation sites for Mg/MgH₂ [21,22], thus improving low-temperature dehydrogenation kinetics. The introduction of TMO_x not only increases the number of active sites but may also stabilize the interfacial structure, mitigating the structural degradation of MgH₂ during cycling. The Ti-MgO and TMO_x catalysts provide additional active sites, accelerating the dehydrogenation and re-hydrogenation processes of MgH₂. Optimal catalyst design can not only increase reaction rates but also facilitate effective hydrogen absorption and desorption at lower temperatures, enhancing the practicality and energy efficiency of Mg/MgH₂. In summary, the synergistic effects of the Ti-

MgO and TMO_x catalysts enhance the kinetic performance and cyclic stability of MgH₂.

4. Conclusions

In summary, we successfully synthesized TMO_x @Ti-MgO ($TM = Mn$ and Cu) composite catalysts, which significantly improve the de/hydrogenation kinetics of MgH₂. The synergistic interaction between Ti-MgO and TMO_x enhances hydrogen adsorption, dissociation and diffusion simultaneously, facilitating low-temperature reversible hydrogen storage. Our findings demonstrate that MgH₂ catalyzed by TMO_x @Ti-MgO releases over 6 wt. % H₂ within 5 min at 280 °C, and exhibits notable hydrogen desorption at 180 °C, with the release rates of 0.89–1.12 wt. % H₂ within 60 min. The composite catalysts maintain high chemical and catalytic stability, preserving hydrogen storage efficiency over 30 cycles. This research presents a strategic approach to overcoming traditional limitations of Ti-based catalysts, offering promising pathways for advanced hydrogen storage materials with enhanced performance and stability.

Data availability

All data generated or analyzed during this study are included in this published article.

Declaration of competing interest

The authors declare the following financial interests/personal relationships which may be considered as potential competing interests:

Prof. Pan is the editor-in-chief for Journal of Magnesium and Alloys. Prof. Pan was not involved in the editorial review or the decision to publish this article. All authors declare that there are no competing interests.

CRediT authorship contribution statement

Haotian Guan: Writing – original draft, Investigation, Formal analysis, Data curation. **Jiang Liu:** Writing – original draft, Investigation. **Qian Li:** Supervision. **Yangfan Lu:** Writing – review & editing, Supervision, Investigation, Funding acquisition, Conceptualization. **Fusheng Pan:** Supervision.

Acknowledgments

This work was supported by the National Key R&D Program of China (2023YFB3809101) and the Fundamental Research Funds for the Central Universities (2023CD-JKYJH005). Q.L. acknowledges the support from the National Natural Science Foundation of China (U23A20128) and Chongqing Science and Technology Commission (CSTC2024YCJH-BGZXM0041).

Supplementary materials

Supplementary material associated with this article can be found, in the online version, at doi:10.1016/j.jma.2025.02.032.

References

- [1] G. Han, Y. Lu, H. Jia, Z. Ding, L. Wu, Y. Shi, G. Wang, Q. Luo, Y.a. Chen, J. Wang, G. Huang, X. Zhou, Q. Li, F. Pan, J. Magnes. Alloy. 11 (2023) 3896–3925.
- [2] Y. Shang, C. Pistidda, G. Gizer, T. Klassen, M. Dornheim, J. Magnes. Alloy. 9 (2021) 1837–1860.
- [3] Y. Yang, X. Xiong, J. Chen, X. Peng, D. Chen, F. Pan, J. Magnes. Alloy. 9 (2021) 705–747.
- [4] H. Wang, J. Li, X. Wei, Y. Zheng, S. Yang, Y. Lu, Z. Ding, Q. Luo, Q. Li, F. Pan, Adv. Funct. Mater. 34 (2024) 2406639.
- [5] Q. Li, Y. Lu, Q. Luo, X. Yang, Y. Yang, J. Tan, Z. Dong, J. Dang, J. Li, Y. Chen, B. Jiang, S. Sun, F. Pan, J. Magnes. Alloy. 9 (2021) 1922–1941.
- [6] Q. Luo, J. Li, B. Li, B. Liu, H. Shao, Q. Li, J. Magnes. Alloy. 7 (2019) 58–71.
- [7] Y. Xinglin, L. Xiaohui, Z. Jiaqi, H. Quanhui, Z. Junhu, Mater. Today Adv. 19 (2023) 100387.
- [8] Z. Han, Y. Wu, H. Yu, S. Zhou, J. Magnes. Alloy. 10 (2022) 1617–1630.
- [9] X. Zhou, J. Li, H. Guan, J. Liu, H. Lu, Y. Zhao, Y.a. Chen, J. Wang, Q. Li, Y. Lu, F. Pan, J. Phys. Chem. Lett. 15 (2024) 8773–8780.
- [10] X. Zhou, H. Guan, H. Lu, Y. Lu, J. Li, J. Wang, Q. Li, F. Pan, J. Magnes. Alloy. (2023), doi:10.1016/j.jma.2023.09.016.
- [11] L. Ren, Y. Li, Z. Li, X. Lin, C. Lu, W. Ding, J. Zou, Nano-Micro Lett 16 (2024) 160.
- [12] J. Zhang, W. Wang, X. Chen, J. Jin, X. Yan, J. Huang, J. Am. Chem. Soc. 146 (2024) 10432–10442.
- [13] M. Pozzo, D. Alfè, Int. J. Hydrogen Energy 34 (2009) 1922–1930.
- [14] X. Zhang, X. Zhang, L. Zhang, Z. Huang, F. Fang, Y. Yang, M. Gao, H. Pan, Y. Liu, J. Mater. Sci. Technol. 144 (2023) 168–177.
- [15] V.V. Berezovets, R.V. Denys, I.Y. Zavaliv, Y.V. Kosarchyn, Int. J. Hydrogen Energy 47 (2022) 7289–7298.
- [16] J. Cui, H. Wang, J. Liu, L. Ouyang, Q. Zhang, D. Sun, X. Yao, M. Zhu, J. Mater. Chem. A 1 (2013) 5603–5611.
- [17] J. Cui, J. Liu, H. Wang, L. Ouyang, D. Sun, M. Zhu, X. Yao, J. Mater. Chem. A 2 (2014) 9645–9655.
- [18] H. Lu, J. Li, Y. Lu, Y.a. Chen, T. Xie, X. Zhou, Q. Li, F. Pan, Int. J. Hydrogen Energy 47 (2022) 38282–38294.
- [19] H. Gao, R. Shi, J. Zhu, Y. Liu, Y. Shao, Y. Zhu, J. Zhang, L. Li, X. Hu, Appl. Surf. Sci. 564 (2021) 150302.
- [20] H. Guan, Y. Lu, J. Liu, Y. Ye, Q. Li, F. Pan, ACS Catal. 14 (2024) 17159–17170.
- [21] H. Wan, S. Zhou, D. Wei, J. Qiu, Z. Ding, Y.a. Chen, J. Wang, F. Pan, Sep. Purif. Technol. 355 (2025) 129776.
- [22] A. Jubair, M.A. Rahman, M.M.R. Khan, M.W. Rahman, Environ. Prog. Sustain. Energy 42 (2023) e13940.
- [23] D. Lee, I. Kwon, J.-L. Bobet, M.Y. Song, J. Alloys Compd. 366 (2004) 279–288.
- [24] J. Sharp, G. Brindley, B.N. Achar, J. Am. Chem. Soc. 49 (1966) 379–382.
- [25] L.F. Jones, D. Dollimore, T. Nicklin, Thermochim. Acta 13 (1975) 240–245.
- [26] L. Ren, W. Zhu, Y. Li, X. Lin, H. Xu, F. Sun, C. Lu, J. Zou, Nano-Micro Lett 14 (2022) 144.
- [27] Y. Shao, H. Gao, Q. Tang, Y. Liu, J. Liu, Y. Zhu, J. Zhang, L. Li, X. Hu, Z. Ba, Appl. Surf. Sci. 585 (2022) 152561.
- [28] P. Wang, Z. Tian, Z. Wang, C. Xia, T. Yang, X. Ou, Int. J. Hydrogen Energy 46 (2021) 27107–27118.
- [29] K. Kajiwara, H. Sugime, S. Noda, N. Hanada, J. Alloys Compd. 893 (2022) 162206.

- [30] Y. Meng, S. Ju, W. Chen, X. Chen, G. Xia, D. Sun, X. Yu, *Small Struct.* 3 (2022) 2200119.
- [31] D. Pukazhselvan, J. Perez, N. Nasani, I. Bdikin, A.V. Kovalevsky, D.P. Fagg, *ChemPhysChem* 17 (2016) 178–183.
- [32] K. Xian, M. Wu, M. Gao, S. Wang, Z. Li, P. Gao, Z. Yao, Y. Liu, W. Sun, H. Pan, *Small* 18 (2022) 2107013.
- [33] X. Huang, X. Xiao, X. Wang, C. Wang, X. Fan, Z. Tang, C. Wang, Q. Wang, L. Chen, L. Chen, *J. Phys. Chem. C* 122 (2018) 27973–27982.
- [34] J. Li, R. Zou, Y. Cui, G. Lei, Z. Li, H. Cao, *Chem. Eng. J.* 470 (2023) 144259.
- [35] Y. Qin, J. Hu, Z. Yang, C. Han, S. Long, D. Zhang, F. Pan, *J. Magnes. Alloy* (2024), doi:10.1016/j.jma.2024.02.012.
- [36] Z. Lan, H. Fu, R. Zhao, H. Liu, W. Zhou, H. Ning, J. Guo, *Chem. Eng. J.* 431 (2022) 133985.
- [37] M. Polanski, J. Bystrzycki, T. Plocinski, *Int. J. Hydrogen Energy* 33 (2008) 1859–1867.
- [38] C. Yan, H.-y. Zhang, F.-y. Wu, S. Ze, J.-g. Zheng, L.-t. Zhang, L.-x. Chen, *Tran. Nonferrous Met. Soc. China* 31 (2021) 3469–3477.
- [39] L. Zhang, Z. Sun, Z. Yao, L. Yang, N. Yan, X. Lu, B. Xiao, X. Zhu, L. Chen, *Nanoscale Adv* 2 (2020) 1666–1675.
- [40] P. Li, Q. Wan, Z. Li, F. Zhai, Y. Li, L. Cui, X. Qu, A.A. Volinsky, *J. Power Sources* 239 (2013) 201–206.
- [41] L. Zhang, L. Ji, Z. Yao, N. Yan, Z. Sun, X. Yang, X. Zhu, S. Hu, L. Chen, *Int. J. Hydrogen Energy* 44 (2019) 21955–21964.
- [42] H. Wan, D. Fang, S. Zhou, X. Yang, Y. Dai, L. Ran, F. Pan, *Int. J. Hydrogen Energy* 48 (2023) 34180–34191.
- [43] J. Mao, Z. Guo, X. Yu, H. Liu, Z. Wu, J. Ni, *Int. J. Hydrogen Energy* 35 (2010) 4569–4575.
- [44] P. Yao, Y. Jiang, Y. Liu, C. Wu, K.-C. Chou, T. Lyu, Q. Li, *J. Magnes. Alloy* 8 (2020) 461–471.
- [45] Q. Zhang, L. Zang, Y. Huang, P. Gao, L. Jiao, H. Yuan, Y. Wang, *Int. J. Hydrogen Energy* 42 (2017) 24247–24255.
- [46] Z. Ma, J. Zhang, Y. Zhu, H. Lin, Y. Liu, Y. Zhang, D. Zhu, L. Li, *ACS Appl. Energy Mater.* 1 (2018) 1158–1165.
- [47] M. Verón, H. Troiani, F. Gennari, *Carbon N Y* 49 (2011) 2413–2423.
- [48] L. Li, G. Jiang, H. Tian, Y. Wang, *Int. J. Hydrogen Energy* 42 (2017) 28464–28472.
- [49] C. Xu, H.J. Lin, J. Liu, P. Zhang, Y. Meng, Y. Liu, J. Zhang, L. Li, Y. Zhu, *ChemistrySelect* 4 (2019) 7709–7714.
- [50] Y. Zhao, Z. Liu, J. Liu, Y. Zhu, J. Zhang, Y. Liu, X. Hu, L. Li, J. Magnes. Alloy. 8 (2022) 461–471.
- [51] N. Xu, H. Zhou, M. Zhang, Y. Ye, K. Wang, Y. Zhou, Y. Zhu, Y. Zhang, *J. Mater. Sci. Technol.* 191 (2024) 49–62.
- [52] H. Huang, T. Xu, J. Chen, J. Yuan, W. Yang, B. Liu, B. Zhang, Y. Wu, *Chem. Eng. J.* 483 (2024) 149434.
- [53] Z. Yuan, S. Li, K. Wang, N. Xu, W. Sun, L. Sun, H. Cao, H. Lin, Y. Zhu, Y. Zhang, *Chem. Eng. J.* 435 (2022) 135050.
- [54] C. Duan, J. Wu, P. Liang, H. Wang, T. Qu, Y. Fan, Y. Su, Z. Su, L. Hu, Y. Wu, *Energy Fuels* 38 (2024) 8979–8991.
- [55] N. Mustafa, N. Juahir, F.H. Yap, M. Ismail, *Int. J. Electroactive Mater.* 4 (2015) 1–7.
- [56] V. Shukla, T.P. Yadav, *Int. J. Energy Res.* 46 (2022) 12804–12819.